

Article

Not peer-reviewed version

# Comparison Of Backprojection Techniques For Rupture Propagation Modelling Of The Mw=7,8 Earthquake Near Kahramanmaras And Its Mw=7,5 Aftershock Near Elbistan Turkey, 2023

[Dimitrios Nikolopoulos](#)\*, [Mahmood Sultan](#), [Aftab Alam](#), [Demetrios Cantzos](#), [Georgios Priniotakis](#), [Michail Papoutsidakis](#), Farhan Javed, George Prezerakos, Jamil Siddique, Muhammad Ali Shah, [Muhammad Rafique](#), [Panayiotis H. Yannakopoulos](#)

Posted Date: 26 February 2025

doi: 10.20944/preprints202502.2064.v1

Keywords: High frequency seismic radiation; Teleseismic Array; Turkey earthquake; Rupture propagation; Beamforming; Multi-Signal Classification















Preprints.org is a free multidisciplinary platform providing preprint service that is dedicated to making early versions of research outputs permanently available and citable. Preprints posted at Preprints.org appear in Web of Science, Crossref, Google Scholar, Scilit, Europe PMC.

Copyright: This open access article is published under a Creative Commons CC BY 4.0 license, which permit the free download, distribution, and reuse, provided that the author and preprint are cited in any reuse.

## Article

# Comparison of Backprojection Techniques for Rupture Propagation Modelling of the $M_w=7,8$ Earthquake Near Kahramanmaras and Its $M_w=7,5$ Aftershock Near Elbistan Turkey, 2023

Dimitrios Nikolopoulos<sup>1,\*</sup> , Mahmood Sultan<sup>2</sup> , Aftab Alam<sup>2</sup> , Demetrios Cantzos<sup>1</sup> , Georgios Priniotakis<sup>1</sup> , Michail Papoutsidakis<sup>1</sup> , Farhan Javed<sup>2</sup> , Georgios Prezerakos<sup>3</sup> , Jamil Siddique<sup>4</sup> , Muhammad Ali Shah<sup>2</sup> , Muhammad Rafique<sup>5</sup>  and Panayiotis Yannakopoulos<sup>3</sup> 

<sup>1</sup> University of West Attica Department of Industrial Design and Production Engineering, Petrou Ralli & Thivon 250, Aigaleo, GR-12244, Athens, Greece

<sup>2</sup> Centre for Earthquake Studies, National Centre for Physics, Shahdra Valley Road, P.O. Box No. 2141, Islamabad 44000, Pakistan

<sup>3</sup> Department of Informatics and Computer Engineering, University of West Attica, Agiou Spyridonos, GR-12243 Aigaleo, Greece

<sup>4</sup> Department of Earth Sciences, Quaid-i-Azam University, Islamabad 44000, Pakistan

<sup>5</sup> Department of Physics King Abdullah Campus, University of Azad Jammu and Kashmir Muzaffarabad, Azad Kashmir, Pakistan

\* Correspondence: dniko@uniwa.gr; Tel.: +0030-210-5381338

**Abstract:** This paper utilises teleseismic Z-component data to investigate the rupture's propagation, extent and velocity field for two destructive earthquakes of the East Anatolian Fault Zone (EAFZ); the  $M_w=7,8$  earthquake occurrence near Kahramanmaras on 2023/Feb/06 and its  $M_w=7,5$  major aftershock at Elbistan (Cardak Fault). Both earthquakes have been the most devastating in that tectonic region during the last decades and have caused property damage and human casualties. The extent of the rupture was modelled with high-resolution beamforming and multichannel classification. The teleseismic data were derived from agencies in the US and Canada. The rupture of the  $M_w=7,8$  earthquake was found to be bi-directional towards north-east and south-west. A distance of 299 km was covered in 185 s with varying velocity field values along the main fault, while its splay and the major aftershock, ruptured, also, bi-directionally, to an extent of 150 km within 46 s. The findings provide new insights of the evolution of the spatio-temporal rupture of the EAFZ and may serve as a basis for long-term earthquake hazard planning of the area.

**Keywords:** High frequency seismic radiation; Teleseismic Array; Turkey earthquake; Rupture propagation; Beamforming; Multi-Signal Classification

## 1. Introduction

The evolution of major earthquakes and the rupture's propagation within the earth's crust can be studied using teleseismic data [1–4]. Global teleseismic data is readily available via the Incorporated Research Institutions for Seismology [3,5], while finite fault-models from teleseismic data for major earthquakes can be found in the United States Geological Survey (USGS) institute [6]. Teleseismic data is, however, biased by the distance from the seismic source and the dimension of the fault [3,7,8]. For example, when the source distance is between  $30^\circ$  to  $90^\circ$ , the body waves propagate homogeneously through the lower mantle, whereas the triplication effect of the upper mantle is minimal on the P waveform [8,9]. In addition, the frequencies of the teleseismic waves influence their travelling since the various wave propagation media may have different impedance for each frequency and favourable range of frequencies for traversing waves, attenuating, in this manner,

diversely the incident teleseismic frequencies or even, diminishing some of these. For example, thick lithosphere relates to weak teleseismic attenuation as has been reported from teleseismic maps from the Sichuan Basin, China [10]. Also, weaker teleseismic scattering suggests more homogeneous crustal and uppermost mantle structure, as reported from measurements in the Gulf of Mexico Coastal Plain [11]. Nevertheless, there are also aspects that the teleseismic data pertain to spurious seismic noise in the frequency band from about 0.003 Hz to 1.0 Hz due to primary, secondary microseismicity and hum [3,12,13] and may contain spurious phases stemming from an inhomogeneous source distribution [9]. Therefore, pure teleseismic data should be used with caution in addition to their lack of source imaging information [3,14,15].

Advantageous to pure teleseismic data, the fast source inversion offers timely, precise and rapid source information for earthquake emergency responses and catastrophe assessment [4,16]. Evenly effective to fast inversion, the backprojection techniques are very robust and utilise teleseismic data for earthquake estimations [e.g. 16–20, and references therein]. These techniques project the characteristics of the seismic waves to the back in order to estimate their properties. The backprojection techniques can delineate the coseismic rupture and its propagation [21], something that cannot be done with pure teleseismic data [15]. The backprojection techniques involve arrays of teleseismic waves used for the estimation of the properties of the ruptured affected areas [1,15,17,22,23]. They are based on the seismogram stacking of multi-stations with time reversal [24–26]. Data from multiple neighbouring stations are used to compose an array which is further utilised to extract the underlying seismic signals [1,26,27, and references therein]. The backprojection techniques are based on the high frequency contents of coherent seismic body waves and as a result they do not depend on the structural inhomogeneities of the earth's crust, nor the geometry of existing fault systems [17,28]. Long and stationary signals can be estimated with these techniques. The back projection techniques uncover the propagation extent and can be applied both in time and frequency domains [4,16,17,20,21,29–36]. Different backprojection techniques have different resolutions but all manage to outline the rupture's patterns of earthquake events [1,17,19–21,37–40] and thus facilitate the study of high energy frequency radiation patterns emitted from the seismic source. In backprojection techniques, the hypocentre of an earthquake is considered as a reference point for an array window. Time domain seismic P-waves are then aligned according to their first arrivals. Grid points are selected near the hypocentre. In order to delineate the propagation of the radiated rupture front shifting and slant stacking of high-frequency seismograms are analysed together with stacked waves coherence, time reversal properties and recorded wave front curvature [1,17,24,25]. The epicentre information is pre-set prior to data processing. Time delays of the waveforms are then projected back, summed up and stacked. The back projected stacked waveform has maximum backprojection power which is used for the estimation of the earthquake's source velocity [17]. The backprojection techniques can delineate the rupture's progress due to earthquakes evolving in the form of multiple fault segments (with or without gaps) with the property to restart after a temporal stop until their termination [1,41]. Back projection techniques are also frequency-dependent and as a result, different subsurface structure favour different frequency components [42]. Note that all back projection techniques depend strongly on near source events and, hence, depend on the near source scatter artefacts i.e., the water and depth phases effects and the 3D velocity structure [17,19,43,44].

Various backprojection techniques have been utilised for array processing in earthquake related rupture, e.g., the surface wave back projection, the cross-correlation technique and the compression sensing method. However, the most prominent backprojection methods are the beamforming and the multiple signal classification (known as MUSIC backprojection technique). Beamforming is the most classical backprojection array processing technique that is focused to the energy of the receiver from the hypocentre of earthquakes [21,45]. MUSIC technique, on the other hand, is based on the estimation of the multitaper cross-spectrum and the coherence data matrix [29] which is used for the differentiation of the spanned subspace that induces an earthquake related signal [46]. As it will be shown in section 2 both methods have been employed in earthquake related signals especially

for the study of the propagation of the rupture that seismicity imposes. Taking into account these fact, this paper utilises beamforming and MUSIC backprojection techniques for the study of two very destructive earthquakes which occurred in Turkey on 2023 (**Figure 1**). The first one is the catastrophic earthquake of  $M_w=7.8$ , Kahramanmaras (Pazarcik) (37.28N and 37.035E) and the second one is the  $M_w=7.5$  earthquake near Elbistan (38.089N and 37.239E), which is considered as the major aftershock of the Kahramanmaras earthquake. The objective is to study the rupture's propagation of these earthquakes, the spatiotemporal extent of the rupture front, as well as, its dimension and its velocity field. To achieve this, back projection is applied on the teleseismic body wave data acquired from thirty two (32) broadband stations of the USArray network of the US in for the  $M_w=7.8$ , Kahramanmaras earthquake and from one hundred and from four (104) broadband stations located in Canada for the  $M_w=7.5$  Elbistan aftershock (**Figure 1**). The one-dimensional AK135 velocity model [47] is employed for the heterogeneous subsurface of both earthquakes. The conventional beamforming and the MUSIC backprojection techniques are employed. As mentioned, both techniques focus to the released seismic energy.

In the following, section 2.4 presents the sources of data and describes the beamforming and MUSIC backprojection techniques. Section 2.1 gives the specific details of the earthquakes under study. The results from the application of both techniques the discussion and the evaluation are presented in section 3.

## 2. Materials and Methods

### 2.1. Geology and Seismic Significance of the Area

The collision of the African and Arabian plates on the south and south-east side of the Anatolian plate form a triple junction [48,49]. The left lateral EAFZ is formed due to break of slabs as the Arabian plate moves northward with overthrust on the Anatolian plate and exerts anti-clockwise rotation to the Anatolian plate [48,50–53]. The EAFZ exhibits a slip rate of  $10 \pm 1 \text{ mm} \cdot \text{year}^{-1}$  [54]. The EAFZ is restricted by the Karliova region on the northeast and by the Kahramanmaras region on the southwest, whereas its total length is 550 km [5,16,55–59]. This plate collision has increased the seismicity in the EAFZ (**Figure 2**). The north-southrending of the Dead Sea Fault Zone (DSFZ), with an estimated length of 1000 km, is also a contributor to the seismicity in the EAFZ [55]. Especially the south end of the DSFZ lies in the Red Sea and, most importantly, its north end merges with the EAFZ at a triple junction point, near the Kahramanmaras region [51,55]. On the south side the Cyprus trench exists due to the compression of the African plate on the Anatolian plate [48,60]. Historical seismicity indicates that the EAFZ was activated through four significant earthquakes of  $M=6.9$  in 1114,  $M_w=7.0$  in 1795,  $M_w=7.2$  in 1872 and  $M_w=7.1$  in 1893 [51,56]. The Kahramanmaras and Elbistan earthquakes are the most important seismic events occurred along the EAFZ since 1939, when the catastrophic  $M_w=7.8$  Erzincan earthquake happened.



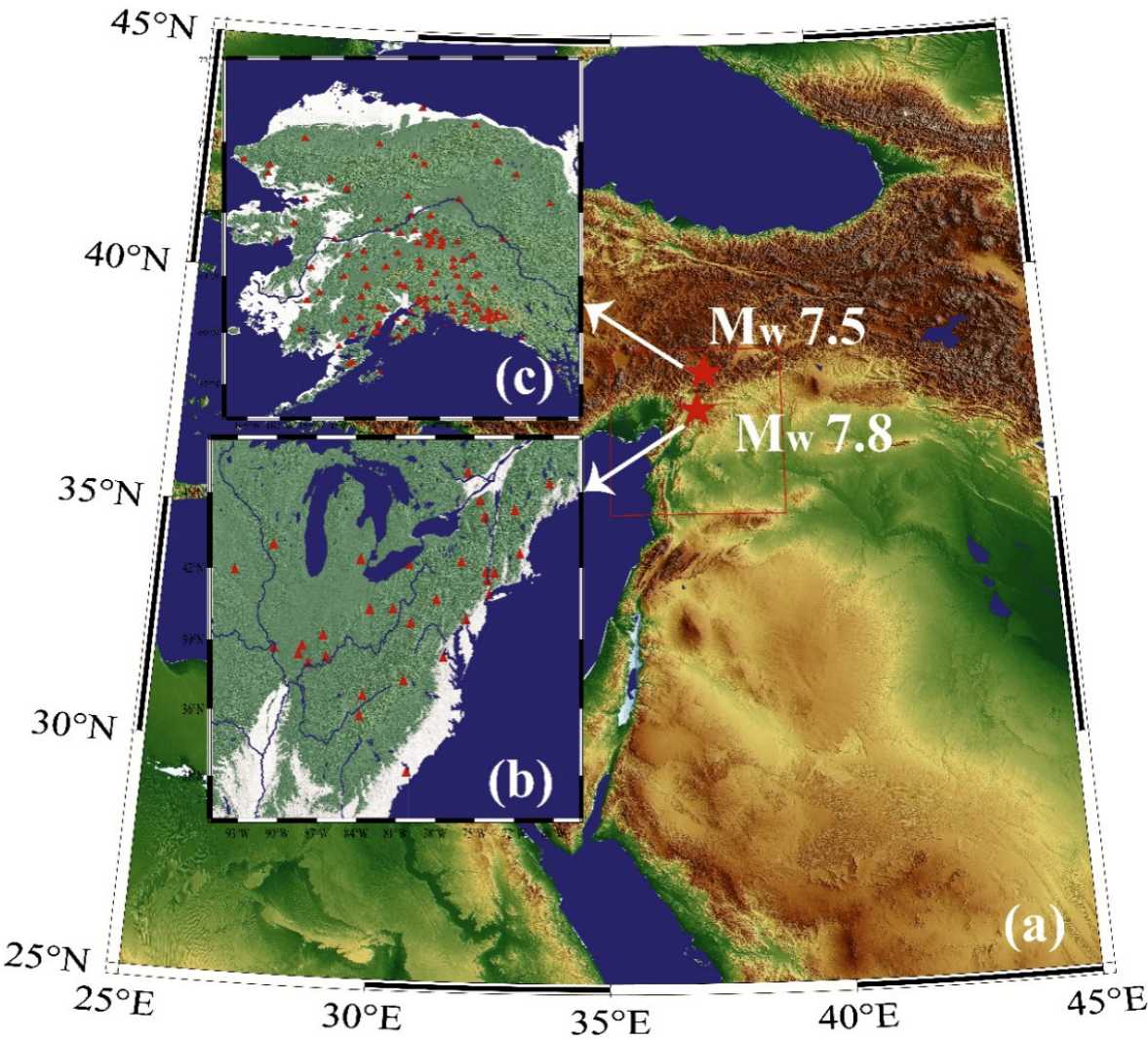


**Figure 1.** Geologic map of the EAFZ. Sub-figure (a): The red stars present the epicentre of the  $M_w=7.8$  Kahramanmaraş earthquake and of its  $M_w=7.5$  Elbistan aftershock. The aerial distance between the epicentres is approximately 100 km. ; (b) Map of the utilised stations of the USArray of the US; (c) Map of the utilised stations of Canada.

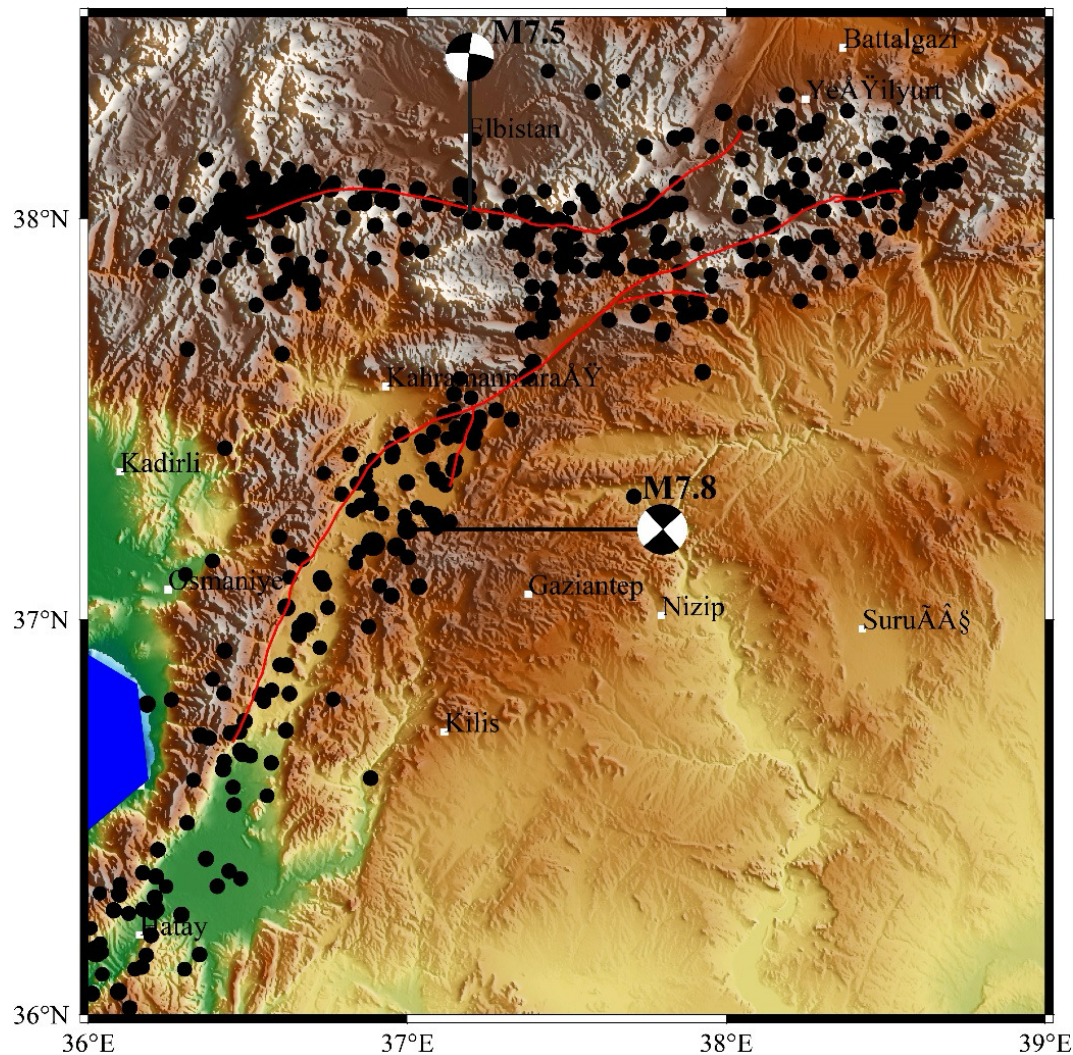


**Figure 2.** The East Anatolian fault system structure, the events under study and the seismicity of the study area.

## 2.2. Beamforming Technique

As a backprojection technique, beamforming projects the characteristics of the seismic waves to the back in order to estimate the properties of the rupture [61]. Beamforming is robust in visualising the rupture's propagation overcoming, simultaneously, through the analysis of the Pn phases of the body waves, the limitations due to the high-frequency content of the source's radiation, both in direction and location, as well as, due to the extent of the rupture. With this technique the seismic phase timing and the arrival's azimuth are estimated from the seismic sub-events of the radiating source [62]. In this way, the wave propagation's pattern and delay are determined, however at a low resolution. Beamforming, additionally calculates the autoprodut phase difference of seismograms from multiple stations even if these exhibit time reversal [45]. By utilising the distinct P waves of coherent signals, beamforming manages to delineate the propagation of the rupture efficiently and with competitive computation performance. It has the ability to extract even weak P wave direct signals from data. Beamforming has an acceptable signal to noise ratio with a resolution defined only by the geometry array [37–40]. However this latter fact limits its potential since it fails to address the swimming artefacts which cause the energy to burst forwards from the geometric array due to the the high frequency content of the large seismic energy released by the sub-events occurring in the earthquake's hypocentre and the sequential trade-off between rupture's time and location [21,45]. Beamforming is applied on the time domain [24,34,45,63]. Beamforming is performed over sliding window against the stacked energy against each point of rupture [64]. To best estimate the source's



amplitude, linear stacking is applied to beamforming data prior to processing[25,65].The beamforming steps are mentioned in Ishii et al. [61].

Regarding earthquake related signals beamforming was employed with success in the 2004  $M_w=9,2$  Sumatra Andaman,Indonesia earthquake,[30,42,43], the 2008  $M_w=7,2$  Wenchuan,China earthquake,[66] the 2005  $M_w=7,6$  Kashmir,Pakistan earthquake [67], the 2010  $M_w= 8,8$  Chile earthquake [37,68], the 2011  $M_w=9,0$  Tohoku, Japan earthquake [69–75,75,76], the 2012  $M_w=8,6$  Sumatra,Indonesia offshore earthquake [44,77–79], in data from Helsinki Area, Southern Finland [80,81], in Salt Lake city,USA[82],in the Gorda plate interface [83],in the Tongzhou, subcenter of Beijing,China [84],in San Juan, Argentina earthquake [85],in long monochromatic earthquake signals [86] as well as,in earthquake related infrasound signals [87,88] and tsunamigenic earthquakes [89]. Beamforming has successfully outlined the earthquake related rupture's length with a maximum of 1300 km(for major earthquakes), as well as, the rupture's extend not exceeding 100 s [90].

### 2.3. MUSIC Backprojection Technique

MUSIC backprojection is a spectral estimation technique based on the covariance matrix of an earthquake related signal. It is a f-k analysis method of filtered waveforms studied via sliding windows. MUSIC backprojection is hence a technique in the frequency domain of the seismic signal. In MUSIC backprojection technique a pseudo-spectrum frequency identifies the arrival's direction from the hypocenter's source with maximum spectrum power [29]. The wave field is converted into plane waves with the seismic covariance matrix eigenvector function. Taking the hypocenter as a reference, sub-events are generated by the phase shifting of the plane waves. With the eigenvalue decomposition, a fine resolution image is produced[62]. In this way manages to minimise the variance of the frequency spectrum of wavenumbers and,consequently, the uncertainties of the seismic phase's arrival time [29]. The direct P-wave's arrival from the filtered waveform is then aligned and hypothesised to originate from in the hypocenter's source.Since P-waves have specific directions and velocities, through the MUSIC backprojection method decomposition, the noise, which exhibits low amplitudes of eigenvalues, is extracted from the signal, which exhibits high amplitudes of eigenvalues. In this way, the MUSIC backprojection technique manages to estimate the steering vector of the source's location and the subspace of the noise in a orthogonal frequency vector space [29]. Through this process, however, the information capacity of raw signal's amplitude, decreases and,as a result, the cross-spectrum is estimated within a narrow frequency band. Thereafter,the covariance matrix of the largest eigenvalue is decomposed with an eigenvector into a subspace signal and its complement into noise subspace [77]. In this way a subspace-spanned signal is defined. During processing with the MUSIC backprojection technique, the arrivals of the the direct P waves are aligned via multiple channel cross-correlation.

The MUSIC backprojection technique estimates well the arrival direction of long and stationary signals [29]. Moreover, the MUSIC backprojection technique addresses the swimming effect which is a major drawback of all other array techniques. The reader should note here that the swimming effect causes the energy to burst in front of the array due to the high frequencies. This is because large seismic energy is released in the high frequencies because of many microcracks self-organising and forming a large cracked region within a sub-event along an earthquake's ray path [77]. The MUSIC backprojection technique offers good resolution for large earthquakes and is capable in distinguishing nearby sources [28].This because it adds a reference station which acts as a window reference for stacking during processing of array data [24,25,62]. Simultaneously, the imaging results of the MUSIC backprojection technique are not affected by the reference station, however, at the expense of computational resources. The MUSIC backprojection technique resolves the rupture's process spatio-temporally, because an earthquake cause multiple faults and of dissimilar focal mechanisms [33]. Note that the conventional backprojection methods cannot easily resolve nearby sources and in this way, MUSIC backprojection technique is advantageous [67].However the most significant gain of the MUSIC backprojection technique is the migration of the swimming effect which is a major artefact of all array techniques [62]. Moreover,the MUSIC backprojection technique estimates well the arrival direction of long and

stationary signals[29]. In addition, the MUSIC backprojection technique resolves the rupture's image well and, surely, way better than the other array techniques [67].

MUSIC backprojection has also been applied to earthquake related signals [29,91,92]. The 2013  $M_w=8.3$  largest deep earthquake at Sea of Okhotsk off the southwest coast of Kamchatka-Kurile slab Peninsula the Russian far east and its sequence has been studied with MUSIC backprojection [29]. Volcanic tremor signals and the earthquakes occurred during the 2014–2015 Holuhraun eruption in Iceland were also investigated with the MUSIC backprojection technique. Fault rupture imaging has been implemented with the MUSIC technique [91]. The 2018–2022 Hualien earthquake sequence, Taiwan has been investigated with the MUSIC backprojection technique [29]. The MUSIC technique has been applied with success to the 2005  $M_w=7.6$  Kashmir earthquake, Pakistan [67]. The 2018  $M_w=7.5$  Palu earthquake-tsunami in the interior of the Molucca sea, Indonesia has been investigated with MUSIC backprojection [22]. The MUSIC technique has been used in the 2016  $M_w=6.4$  Meinong, Taiwan earthquake has been studied [93]. MUSIC backprojection has been applied to 56 earthquakes from 2010 to 2022 with  $M_w \geq 7.5$  and depth less than 200 km [94]. The 2021  $M_w=7.1$  Fukushima earthquake, Japan has also been studied with the MUSIC technique [95].

#### 2.4. Data and Methodology

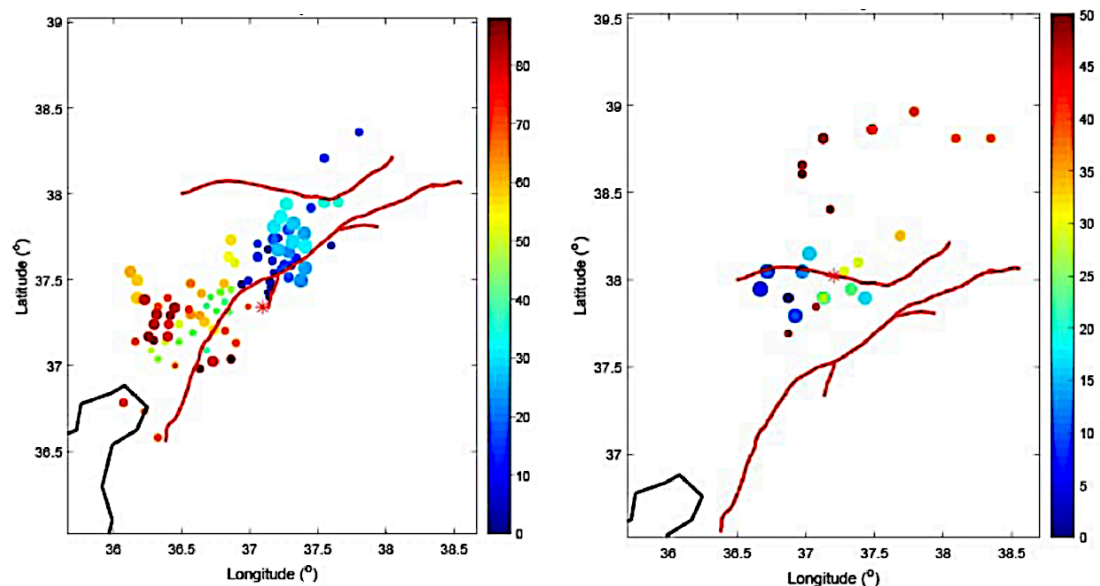
As mentioned in section 1, the array of the seismic data of this paper are acquired from 32 broadband stations of the USArray network of the US and from 104 broadband stations installed in Canada. Both networks are oriented approximately in parallel to the dominant direction of the EAFZ and therefore, the spatial resolution of the acquired data is better along the ruptured fault. Broadband seismic station arrays are derived both for the main  $M_w=7.8$  earthquake and its major  $M_w=7.5$  aftershock. First, the seismograms of the direct P-waveforms with clear reference [30] are aligned through a bandpass frequency filter applied at time  $t = 0s$  (arrival time). This is done by computing the cross-correlation of the first Pn arrivals with 10 s windows [? ], taking into account the hypocenter's latitude, longitude and depth. Through this approach the uncertainties for the structure of velocity are minimized. Note, that these uncertainties may cause errors in estimation of the travel time [30]. Importantly, the seismogram alignment eliminates the delay due to localised side effects [76]. As a result, the energy released from the source is extracted in a compressed form in the frequency domain [76].

Both for the 2023  $M_w=7.8$  Kahramanmaras earthquake and its major  $M_w=7.5$  Elbistan aftershock, the seismograms exhibit a dominant frequency at 0.6 Hz. To cover this frequency, a range of filters is applied between 0.5 Hz and 1 Hz and the P-waveform is aligned using the cross correlation with each earthquake's epicentre as a reference. The source region is then segmented into small grids. The filtered teleseismic P-waveform is thereafter back-projected to the source. The travel time variation due to the earth's structure between the source and the receiver is taken into account during back projection. The velocity of the rupture's front is performed with the 1-D reference model IASP91 [47], both for the main event and its major aftershock. Note, that back projection dominates also at 0.6 Hz and therefore, the 0.6 Hz filter resembles the rupture's shear velocity [96]. Since the resolution of the array of events depends on the waveform's coherence-incoherence and its interference., the filter at 0.6 Hz addresses the time-frequency trade-off and the coherency of the array data and this should be emphasised. Significantly, both earthquakes are taken as an array of sub-events of the event series along the rupture that radiates energy at high frequencies [97]. The MUSIC backprojection technique is applied to the teleseismic data also at a peak frequency of 0.6 Hz [9]. The array network processing and the image generation with the MUSIC backprojection technique enhances temporal evolution. For better resolution with MUSIC backprojection technique the calibration of slowness is carried out [62]. Importantly, cross-spectrum narrow-band estimates are also employed in the MUSIC backprojection technique.



### 3. Results and Discussion

The rupture of the Kahramanmaras and Elbistan earthquakes started with the occurrence of the Kahramanmaras earthquake on 6 of February 2023 and thereafter, propagated and radiated energy along the whole of the activated region of the fault zone [98]. Beamforming identifies three segments for the rupture of the Kahramanmaras earthquake (**Figure 3** as there is a concentration of red-orange yellow points between  $34,5^{\circ}$  and  $37,5^{\circ}$  longitude and  $37,0^{\circ}$  and  $37,5^{\circ}$  latitude along the downward fault (red) line (segment 1), a second concentration of dark blue lines between  $37,0^{\circ}$  and  $37,5^{\circ}$  longitude and around  $37,5^{\circ}$  latitude (segment 2) and the remaining series of mainly cyan points approximately above  $37,0^{\circ}$  longitude and above  $37,5^{\circ}$  latitude (segment 3). Interestingly, segment 2 points are near the Kahramanmaras earthquake's epicentre. As can be observed in **Figure 3, subfigure a**, beamforming is not successful in resolving the extent and the pattern of the rupture because it gives puzzled information regarding both the direction and the limits of the rupture. Indeed in both figures the majority of the data points are away from the activated fault segment (red lines). This may be attributed to the swimming effect and to potential deviations between the actual velocities of the sub-surface and the ones according by the IASP91 model. On the other hand, beamforming successfully distinguishes the rupture's extent from the fault's geometry **Figure 3**. Indeed the black lines which delimit rupture's extent are well away from the red ones for of both sub-figures of **Figure 3, subfigure a**, i.e. this is valid for both the Kahramanmaras earthquake and its aftershock. This can be explained by the fact that the high-frequency coherent P-body waves are related both to the earthquake's triggering and its extend [68,99,100].



(a) Beamforming from the  $M_w=7.8$  Kahramanmaras earthquake data. The red star shows the epicentre of the Kahramanmaras earthquake.

(b) Beamforming from the  $M_w=7.5$  Elbistan aftershock's earthquake data. The red star shows the epicentre of the Elbistan aftershock.

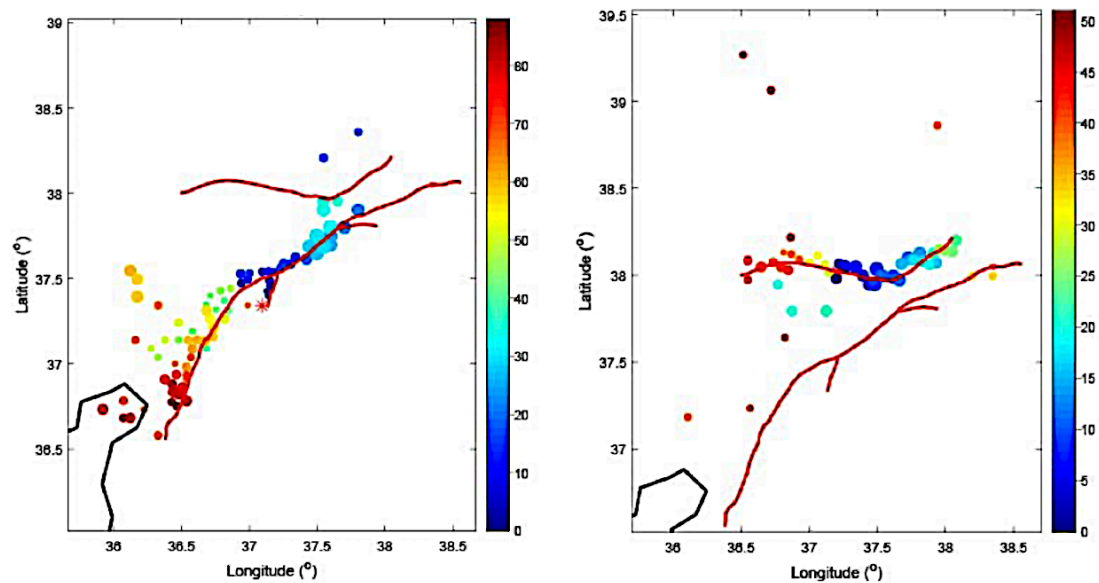
**Figure 3.** Results of the beamforming technique. The coloured scale of the points represents the intensity of the output of beamforming. The red lines represent the activated faults segments

As with beamforming, MUSIC backprojection identifies three segments for the rupture of the Kahramanmaras earthquake (**Figure 4, subfigure a**). The first segment (segment 1) is observed for the concentration of red and orange and some green points between  $36,5^{\circ}$  and  $37,0^{\circ}$  longitude and around  $37^{\circ}$  latitude. The second segment (segment 2) is for the concentration of dark blue points between  $37,0^{\circ}$  and  $37,5^{\circ}$  longitude and around  $37,5^{\circ}$  latitude. This segment is also near the Kahramanmaras earthquake's epicentre and this should be emphasised. It is significant and should be pointed out, that both beamforming and MUSIC backprojection technique coincide in the longitude-latitude and intensity findings from the dark blue points around the earthquake's epicentre. The third segment (segment

3) is for the concentration of light blue-cyan points approximately above  $37,0^{\circ}$  longitude and above  $37,5^{\circ}$  latitude, importantly, at the same longitude-latitude ranges as the ones of segment 3 points from the beamforming technique. However, in both **Figure 3, subfigure a** (beamforming Kahramanmaras earthquake's results) and **Figure 4, subfigure a** (MUSIC backprojection's Kahramanmaras earthquake's results) there are points that are away from the downward fault (red) line, indicating rupture's spatial discrepancies for both techniques. This is more pronounced for the results of the backprojection's technique. As has been explained already in several parts of the text above, MUSIC backprojection is advantageous for the investigation of the rupture of earthquakes [e.g. 93, and references therein]

The Elbistan aftershock evokes in the upward fault three more segments in the outcomes from the application of MUSIC backprojection **Figure 4, subfigure b**. The first segment (segment 1) is found between  $36,5^{\circ}$  and  $37,0^{\circ}$  longitude and around  $38^{\circ}$  latitude where red and orange points concentrate. The second segment (segment 2) is observed as a concentration of dark blue points around  $37,5^{\circ}$  longitude and  $38,0^{\circ}$  latitude. This segment is also near the Elbistan aftershock's epicentre. The third segment (segment 3) is found as a concentration of light blue-cyan and green points around  $38,0^{\circ}$  longitude and latitude. Only six points deviate from the upward fault (red) line, whereas two points are in the downward fault line. Beamforming rather fails to discriminate these segments. Only some dark blue, cyan and green points are within the upward fault line. However, there is a discrete concentration of red-orange points between  $37,0^{\circ}$  and  $38,5^{\circ}$  longitude and between  $38,5^{\circ}$  and  $39,0^{\circ}$  longitude. In this sense beamforming seems to discriminate two segments.

Both backprojection techniques identify discrete intensity segments. Five (5) total segments are found by beamforming while MUSIC backprojection technique identifies six (6) segments. This is in line with the international literature. Indeed as already mentioned, backprojection suffers from artefacts due to swimming effects whereas MUSIC backprojection is not sensitive to these [1,24,29,45,62,88,93]. As already mentioned the swimming effects are a significant factor of point deviations between these two techniques because they cause the seismic energy to burst in front of the array of stations' data due to the high frequencies contribution [17,22,24,29]. Another mentioned reason is potential the deviation between the actual velocities of the sub-surface and those calculated by the IASP91 model [2,6,43,58,66,94]. As both backprojection techniques indicate, some intensity points are scattered and away from the points' mainstream. This is more or less expected since the evolution of both Kahramanmaras and Elbistan earthquakes were complex [54,57,59,101] and as a result the rupture's evolution is hard to predict fully. Moreover, the progress of earthquakes follow fractal patterns of self-organised criticality [102] and as a result the rupture's progress can be strongly biased by these physical pathways adding more deviation to the results data. On the other hand, both beamforming and MUSIC backprojection technique coincide in the longitude-latitude and intensity findings from the dark blue points around the earthquakes and especially near both epicentres. This is also significant and should be emphasised. For both earthquakes, the beamforming and MUSIC backprojection techniques indicate a main concentration points being along the direction of the dissipation of the energy.



(a) MUSIC backprojection technique application to the  $M_w=7.8$  Kahramanmaras earthquake data. The red star shows the epicentre of the Kahramanmaras earthquake.

(b) MUSIC backprojection technique application to the  $M_w=7.5$  Elbistan aftershock's earthquake data. The red star shows the epicentre of the Elbistan aftershock.

**Figure 4.** Results of the MUSIC backprojection technique. The coloured scale of the points represents the intensity of the output of the MUSIC technique. The red lines represent the activated faults segments

The rupture's velocities of the segments of both events can be calculated by estimating the slip rate through the corresponding slip model of each ruptured patch [96]. Through this approach the velocities of the rupture are divided in six (6) velocity segments (Figure 5). Three velocity segments of the downward fault (segments 1, 2a, 2b and 3) are due to  $M_w=7.8$  Kahramanmaras earthquake and the remaining segments (segments 4 and 5) are in the upward fault line and due to  $M_w=7.5$  Elbistan aftershock. Since the  $M_w=7.8$  Kahramanmaras earthquake was generated at the splay of the EAFZ 16 km away from the main fault, the rupture initiating from the earthquake's epicentre covered the 16 km distance in 6 s. That occurred in the first velocity segment and moved towards the main EAFZ. In the second velocity segment, the rupture exhibited a bi-directional pattern on the north-east and south-west sides but yields different velocities, possibly, due to lithological differences. Therefore, the second velocity segment is divided into two sub-segments, namely segment 2a (north-east side) and segment 2b (south-west side). The segment 2a covered the 108 km distance of along the main fault along the north-east direction in 35 s with an average velocity of 3.1 km/s. Simultaneously, the rupture propagated in the south-west side namely, segment 2b covered the distance of 35 km in 10.5 s with an average velocity of 3.4 km/s. After covering the distance of 35 km kilometres, the 2b segment's rupture was momentarily blocked. For segment 2b the average velocity is near to super-shear velocity, i.e., it is a sub-shear velocity. After 41 s the 3rd segment initiated along the south side of the main fault. The direction of segment 3 is south-east with a dominant direction southwards. This process continued for the next 42 s and covered the distance of 140 km before the rupture arrest. Segment 3 has an average velocity of 3.3 km/sec as shown in Figure 5. Therefore, these segment rupture seizures may be due to the transition zone of brittle-ductile subsurface material along the fault. The Elbistan major aftershock was a left-lateral strike-slip fault [58,59,101] that occurred 9 h and 7 min after the main event and propagated in both directions from the epicentre. The first phase of this aftershock corresponds to segment 4. Its rupture propagated along the north-east direction with an average velocity of 3.21 km/s. The duration of this segment was 28 s and covered 90 km distance. The rupture re-initiated from the epicentre in segment 5 along the south-west direction. It attained an average velocity of 3.4 km/s which approaches a super shear velocity (Figure 5). This may be due to its strike-slip nature [64]. The

total distance covered in this segment is 60 km with a duration of 17,5 s before the rupture stopped. Hence the total rupture's velocity is of 3,2 km/s. **Table 1** presents the information of all the segments.

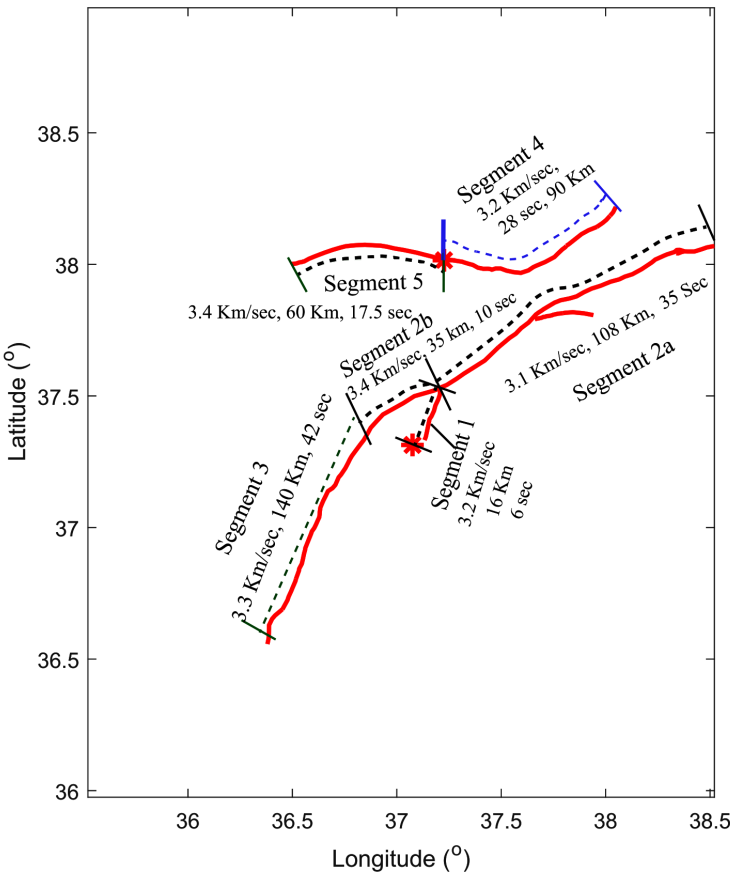


**Figure 5.** The delimited rupture segments of the Kahramanmaras and Elbistan earthquakes.

**Table 1.** Results from the investigated techniques for both earthquakes under study

<i>M<sub>w</sub></i> =7,8 Kahramanmaras Earthquake				
Segment	Distance (Km)	Time (sec)	Velocity (Km/sec)	Direction
1	16	6	3,2	North
2 a	108	35	3.1	North-east
2 b	35	10.5	3,4	South-west
3	140	42	3,3	South-west
<i>M<sub>w</sub></i> =7,5 Elbistan earthquake				
4	90	28	3,2	North-east
5	60	17.5	3,4	South-west

From the above data it becomes evident that both earthquake events attain on average sub and super shear velocity. It is interesting that sub and super shear velocity has been reported for the same earthquake doublet also by a recent publication [58]. Super-shear velocity was observed in the 2002 Denali fault earthquake [103], in the 2010 Qinghai, China, earthquake [104], in the 2013 Craig, Alaska *M<sub>w</sub>*=7,5 earthquake [105], in the *M<sub>w</sub>*=6,7 aftershock of the 2013 Sea of Okhotsk earthquake [106], in several short-period earthquakes [94], in laboratory earthquakes along inhomogeneous faults [107] and in several oceanic and continental earthquakes [63]. It should be mentioned here that both earthquakes have bilateral rupture's propagation but, as mentioned above, with different velocities and segments. According to the findings. the rupture nucleates along the strike. A possible explanation is that the nucleation propagation of the rupture initiates when the strength exceeds the strength of the fault and this happens when the strength of the rupture exceeds the friction of the fault, which is the barrier for



the propagation of the rupture [108]. This means, in turn, that the ruptured segments of the fault along the main event, may be an indication that the subsurface lithology transit between brittle and ductile materials. All these occur possibly at the hypocenters of both earthquakes. The rupture's segments are captured in the frequency range between 0.5 Hz and 1.0 Hz indicating a frequency range including, interestingly, the dominant P-wave frequency of 0.6 Hz. At the tip of each segment, the extent of the propagating rupture, more or less, runs into the surrounding lithology, but encounters obstacles because of increased strength at the boundary of the sub surface. and below. This, in turn, makes the first rupture to stagnate and then stop due to the propagation's phase. Both stress and friction of the fault's lane impose damages along the affected area depending on the rupture's velocity and its extent both relating to the properties of fault zone [98]. Estimating the rupture's segmentation, direction, velocity and extent through phase-coherent direct P-waves is a significant approach to delineating earthquake related parameters. Although earthquakes are still hard to forecast [102], the scientific efforts to delineate the associated rupture is of great importance especially for catastrophic earthquakes as the the seismic doublet of Turkey, 2023.

#### 4. Conclusions

In this paper back projection source imaging techniques are utilised for body waves recorded by seismic arrays at regional scale distances via P-direct waves. The employed methods were the conventional beamforming and the MUSIC backprojection. Especially the MUSIC backprojection method was applied with multi-taper cross-spectral estimation to achieve a sharp source imaging. Through these techniques key rupture's aspects were extracted, such as the location and evolution of the high frequency radiation sources of the rupture process. The results indicated that there are phases of approximately super shear rupture velocity both for the main earthquake its major aftershock. At the tip end of rupture's extent, the originated high-frequency radiations arrest. Therefore, the end tip of each segment was delimited along with the extent of the rupture. The direct P-waveforms were filtered in a frequency window including the dominant 0.6 Hz frequency. The beamforming technique was not successful in resolving the rupture's process of any event. In contrary, the MUSIC backprojection technique resolved the segments and quantified the rupture behaviour of both events. This is because the sliding concept of the reference window that was applied in MUSIC backprojection at low frequencies enabled the mitigation of the swimming artefact on the time shift stack, which is a result of the non-stationarity of the recorded signals. The MUSIC backprojection method's results revealed the rupture's and velocity's segments and their process for both the 2023  $M_w=7.8$ , Kahramanmaras earthquake and its major  $M_w=7.5$  Elbistan aftershock. Five velocity segments were identified in the main event with a total distance of 299 km that was covered in 185 s. Two segments were delimited in the major aftershock with a total distance of 150 km covered in 46 s. Comparing beamforming and MUSIC backprojection techniques outputs, the results from MUSIC backprojection techniques are more reliable for validating rupture's processes of both earthquakes under investigation.

#### Evaluation-Limitations

The approach followed in this paper focused on a very important earthquake doublet that occurred recently (2023) in Turkey. These earthquakes imposed significant damages and, only due to this, the investigation of the rupture of these earthquakes makes this paper of interest. Due to the significance of these earthquakes several papers were published for these. A selected set of these is presented in this paper. The investigation included two well accepted techniques with very recent publications on the subject. Both facts add value to this research. The employed techniques have been and are used by investigators for the study of earthquakes' associated rupture and the spatio-temporal characteristics of this. According to presented literature data, numerous medium and big earthquakes have been studied with beamforming and, especially, MUSIC backprojection. The techniques estimated the rupture's spatial characteristics but not the temporal ones. This is a limitation. Rupture and velocity segments were identified and quantified. On the other hand, the 1-D velocity model used is from 1991, despite

still in use. The use of 3-D velocity models will be a future approach, but for this paper it is another limitation. The paper basically concluded that both events are associated with sub and super shear velocity. This was found by other publications and especially for the same earthquake doublet. This is a positive contribution. In general the paper outlined and utilised mainly recent references and showed the scientific interest on this subject. The application of these techniques to more earthquakes is needed to establish its generality and usability.

**Author Contributions:** Conceptualization, D.N., and M.S.; methodology, D.N., A.A.D.C., G.P., M.P. and J.S.; software, Gi.P.D.C., M.P., A.A., M.S. and J.S.; formal analysis, D.N., G.P., M.P., D.C., P.Y., F.J., M.R. and Gi.P.; investigation, D.N., D.C., P.Y., Gi.P., G.P., M.R., M.P., J.S. and M.R.; resources, M.S., A.A., J.S., M.A.S., M.R. and F.J.; data curation, D.N., G.P., M.P., P.Y., Gi.P., M.S. and A.A.; writing—original draft preparation, D.N., M.S., A.A.F.J., J.S. and M.R.; writing—review and editing, D.N., G.P., Gi.P., M.P., P.Y., D.C., M.S., M.R. and A.A.; visualization, M.S.; supervision, D.N., M.R.; project administration, D.N. and A.A.

## References

1. Cao, B.; Ge, Z. Cascading multi-segment rupture process of the 2023 Turkish earthquake doublet on a complex fault system revealed by teleseismic P wave back projection method. *Earthquake Science* **2024**, *37*, 158–173. <https://doi.org/https://doi.org/10.1016/j.eqs.2024.01.017>.
2. Hayes, G.P. The finite, kinematic rupture properties of great-sized earthquakes since 1990. *Earth and Planetary Science Letters* **2017**, *468*, 94–100. <https://doi.org/https://doi.org/10.1016/j.epsl.2017.04.003>.
3. Mendoza, C.; Hartzell, S.; Ramirez-Guzman, L.; Martinez-Lopez, R. Prediction of Regional Broadband Strong Ground Motions Using a Teleseismic Source Model of the 18 April 2014 Mw 7.3 Papanao, Mexico, Earthquake. *Bulletin of the Seismological Society of America* **2024**, *114*, 2524–2545. <https://doi.org/10.1785/0120230311>.
4. Xu, C.; Zhang, Y.; Hua, S.; Zhang, X.; Xu, L.; Chen, Y.; Taymaz, T. Rapid source inversions of the 2023 SE Türkiye earthquakes with teleseismic and strong-motion data. *Earthquake Science* **2023**, *36*, 316–327. <https://doi.org/https://doi.org/10.1016/j.eqs.2023.05.004>.
5. Taymaz, T.; Ganas, A.; Yolsal-Çevikbilen, S.; Vera, F.; Eken, T.; Erman, C.; Keleş, D.; Kapetanidis, V.; Valkaniotis, S.; Karasante, I.; et al. Source mechanism and rupture process of the 24 January 2020 Mw 6.7 Doğanlı-Sivrice earthquake obtained from seismological waveform analysis and space geodetic observations on the East Anatolian Fault Zone (Turkey). *Tectonophysics* **2021**, *804*, 228745. <https://doi.org/https://doi.org/10.1016/j.tecto.2021.228745>.
6. Goldberg, D.E.; Koch, P.; Melgar, D.; Riquelme, S.; Yeck, W.L. Beyond the Teleseism: Introducing Regional Seismic and Geodetic Data into Routine USGS Finite-Fault Modeling. *Seismological Research Letters* **2022**, *93*, 3308–3323. <https://doi.org/10.1785/0220220047>.
7. Chelidze, T.; Matcharashvili, T.; Varamashvili, N.; Mepharidze, E.; Tephnadze, D.; Chelidze, Z. 9 - Complexity and Synchronization Analysis in Natural and Dynamically Forced Stick-Slip: A Review. In *Complexity of Seismic Time Series*; Chelidze, T.; Vallianatos, F.; Telesca, L., Eds.; Elsevier, 2018; pp. 275–320. <https://doi.org/https://doi.org/10.1016/B978-0-12-813138-1.00009-2>.
8. Ringler, A.T.; Anthony, R.E.; Aster, R.C.; Ammon, C.J.; Arrowsmith, S.; Benz, H.; Ebeling, C.; Frassetto, A.; Kim, W.Y.; Koelemeijer, P.; et al. Achievements and Prospects of Global Broadband Seismographic Networks After 30 Years of Continuous Geophysical Observations. *Reviews of Geophysics* **2022**, *60*, e2021RG000749. <https://doi.org/https://doi.org/10.1029/2021RG000749>.
9. Kato, S.; Nishida, K. Extraction of Mantle Discontinuities From Teleseismic Body-Wave Microseisms. *Geophysical Research Letters* **2023**, *50*, e2023GL105017. <https://doi.org/https://doi.org/10.1029/2023GL105017>.
10. Deng, Y.; Byrnes, J.S.; Bezada, M. New Insights Into the Heterogeneity of the Lithosphere-Asthenosphere System Beneath South China From Teleseismic Body-Wave Attenuation. *Geophysical Research Letters* **2021**, *48*, e2020GL091654. <https://doi.org/https://doi.org/10.1029/2020GL091654>.
11. Shrivastava, A.; Liu, K.H.; Gao, S.S. Teleseismic P-Wave Attenuation Beneath the Southeastern United States. *Geochemistry, Geophysics, Geosystems* **2021**, *22*, e2021GC009715. <https://doi.org/https://doi.org/10.1029/2021GC009715>.
12. Li, L.; Boué, P.; Campillo, M. Observation and explanation of spurious seismic signals emerging in teleseismic noise correlations. *Solid Earth* **2020**, *11*, 173–184. <https://doi.org/10.5194/se-11-173-2020>.

13. Li, B.; Wu, B.; Bao, H.; Oglesby, D.D.; Ghosh, A.; Gabriel, A.A.; Meng, L.; Chu, R. Rupture Heterogeneity and Directivity Effects in Back-Projection Analysis. *Journal of Geophysical Research: Solid Earth* **2022**, *127*, e2021JB022663. <https://doi.org/https://doi.org/10.1029/2021JB022663>.
14. Song, X. Seismic array imaging of teleseismic body waves from finite-frequency tomography to full waveform inversions: with applications to south-central Alaska subduction zone. PhD thesis, Graduate Department of Physics, University of Toronto, 2019.
15. Yin, J.; Denolle, M.A. Relating teleseismic backprojection images to earthquake kinematics. *Geophysical Journal International* **2019**, *217*, 729–747. <https://doi.org/10.1093/gji/ggz048>.
16. Zhang, Y.; Tang, X.; Liu, D.; Taymaz, T.; Eken, T.; Guo, R.; Zheng, Y.; Wang, J.; Sun, H. Geometric controls on cascading rupture of the 2023 Kahramanmaraş earthquake doublet. *Nature Geoscience* **2023**, *16*, 1054–1060. <https://doi.org/10.1038/s41561-023-01283-3>.
17. Du, H. Estimating rupture front of large earthquakes using a novel multi-array back-projection method. *Frontiers in Earth Science* **2021**, *9*, 680163. <https://doi.org/https://doi.org/10.3389/feart.2021.680163>.
18. Steinberg, A.; Sudhaus, H.; Krüger, F. Using teleseismic backprojection and InSAR to obtain segmentation information for large earthquakes: a case study of the 2016 Mw 6.6 Muji earthquake. *Geophysical Journal International* **2022**, *232*, 1482–1502. <https://doi.org/10.1093/gji/ggac392>.
19. Meng, L.; Zhang, A.; Yagi, Y. Improving back projection imaging with a novel physics-based aftershock calibration approach: A case study of the 2015 Gorkha earthquake. *Geophysical Research Letters* **2016**, *43*, 628–636.
20. Zhang, H.; Koper, K.D.; Pankow, K.; Ge, Z. Imaging the 2016 Mw 7.8 Kaikoura, New Zealand, earthquake with teleseismic P waves: A cascading rupture across multiple faults. *Geophysical Research Letters* **2017**, *44*, 4790–4798.
21. Meng, L.; Bao, H.; Huang, H.; Zhang, A.; Bloore, A.; Liu, Z. Double pincer movement: Encircling rupture splitting during the 2015 Mw 8.3 Illapel earthquake. *Earth and Planetary Science Letters* **2018**, *495*, 164–173.
22. Fahmi, M.N.; Realita, A.; Risanti, H.; Prastowo, T.; Madlazim. Back-projection results for the M w 7.5, 28 September 2018 Palu earthquake-tsunami. *Journal of Physics: Conference Series* **2022**, *2377*. <https://doi.org/10.1088/1742-6596/2377/1/012032>.
23. Xie, Y.; Meng, L.; Zhou, T.; Xu, L.; Bao, H.; Chu, R. The 2021 Mw 7.3 East Cape Earthquake: Triggered Rupture in Complex Faulting Revealed by Multi-Array Back-Projections. *Geophysical Research Letters* **2022**, *49*, e2022GL099643. <https://doi.org/https://doi.org/10.1029/2022GL099643>.
24. Claudino, C.; Lupinacci, W.M. The spectral stacking method and its application in seismic data resolution increase. *Geophysical Prospecting* **2023**, *71*, 509–517. <https://doi.org/https://doi.org/10.1111/1365-2478.13335>.
25. Lai, H.; Garnero, E.J. Travel time and waveform measurements of global multibounce seismic waves using virtual station seismogram stacks. *Geochemistry, Geophysics, Geosystems* **2020**, *21*, e2019GC008679. <https://doi.org/https://doi.org/10.1029/2019GC008679>.
26. Wu, H.; Xiao, W.; Ren, H. Automatic time picking for weak seismic phase in the strong noise and interference environment: An hybrid method based on array similarity. *Sensors* **2022**, *22*, 9924. <https://doi.org/https://doi.org/10.3390/s22249924>.
27. Xie, Y.; Bao, H.; Meng, L. Source Imaging With a Multi-Array Local Back-Projection and Its Application to the 2019 Mw 6.4 and Mw 7.1 Ridgecrest Earthquakes. *Journal of Geophysical Research: Solid Earth* **2021**, *126*, e2020JB021396. <https://doi.org/https://doi.org/10.1029/2020JB021396>.
28. Kiser, E.; Ishii, M. Back-projection imaging of earthquakes. *Annual Review of Earth and Planetary Sciences* **2017**, *45*, 271–299.
29. Jian, P.R.; Wang, Y. Applying unsupervised machine-learning algorithms and MUSIC back-projection to characterize 2018–2022 Hualien earthquake sequence. *Terrestrial, Atmospheric and Oceanic Sciences* **2022**, *33*, 28. <https://doi.org/https://doi.org/10.1785/0220210016>.
30. Ishii, M.; Shearer, P.M.; Houston, H.; Vidale, J.E. Extent, duration and speed of the 2004 Sumatra–Andaman earthquake imaged by the Hi-Net array. *Nature* **2005**, *435*, 933–936.
31. Kiser, E.; Ishii, M. Combining seismic arrays to image the high-frequency characteristics of large earthquakes. *Geophysical Journal International* **2012**, *188*, 1117–1128.
32. Neo, J.C.; Fan, W.; Huang, Y.; Dowling, D. Frequency-difference backprojection of earthquakes. *Geophysical Journal International* **2022**, *231*, 2173–2185. <https://doi.org/10.1093/gji/ggac323>.
33. Zeng, H.; Wei, S.; Wu, W. Sources of uncertainties and artefacts in back-projection results. *Geophysical Journal International* **2019**, *220*, 876–891. <https://doi.org/10.1093/gji/ggz482>.

34. Tan, F.; Ge, Z.; Kao, H.; Nissen, E. Validation of the 3-D phase-weighted relative back projection technique and its application to the 2016 M w 7.8 Kaikōura Earthquake. *Geophysical Journal International* **2019**, *217*, 375–388.
35. Vera, F.; Tilmann, F.; Saul, J.; Evangelidis, C.P. Imaging the 2007 Mw 7.7 Tocopilla earthquake from short-period back-projection. *Journal of South American Earth Sciences* **2023**, *127*, 104399. <https://doi.org/https://doi.org/10.1016/j.jsames.2023.104399>.
36. Zhang, H.; Ge, Z. Stepover rupture of the 2014 M w 7.0 Yutian, Xinjiang, Earthquake. *Bulletin of the Seismological Society of America* **2017**, *107*, 581–591.
37. Liu, Z.; Song, C.; Meng, L.; Ge, Z.; Huang, Q.; Wu, Q. Utilizing a 3D global P-wave tomography model to improve backprojection imaging: A case study of the 2015 Nepal earthquake. *Bulletin of the Seismological Society of America* **2017**, *107*, 2459–2466.
38. Qin, W.; Yao, H. Characteristics of subevents and three-stage rupture processes of the 2015 Mw 7.8 Gorkha Nepal earthquake from multiple-array back projection. *Journal of Asian Earth Sciences* **2017**, *133*, 72–79.
39. Yagi, Y.; Okuwaki, R. Integrated seismic source model of the 2015 Gorkha, Nepal, earthquake. *Geophysical Research Letters* **2015**, *42*, 6229–6235.
40. Zhang, H.; Van Der Lee, S.; Ge, Z. Multiarray rupture imaging of the devastating 2015 Gorkha, Nepal, earthquake sequence. *Geophysical Research Letters* **2016**, *43*, 584–591.
41. Nissen, E.; Elliott, J.; Sloan, R.; Craig, T.; Funning, G.; Hutko, A.; Parsons, B.; Wright, T. Limitations of rupture forecasting exposed by instantaneously triggered earthquake doublet. *Nature Geoscience* **2016**, *9*, 330–336.
42. Bletery, Q.; Sladen, A.; Jiang, J.; Simons, M. A Bayesian source model for the 2004 great Sumatra-Andaman earthquake. *Journal of Geophysical Research: Solid Earth* **2016**, *121*, 5116–5135. <https://doi.org/https://doi.org/10.1002/2016JB012911>.
43. Fan, W.; Shearer, P.M. Coherent seismic arrivals in the P wave coda of the 2012 Mw 7.2 Sumatra earthquake: Water reverberations or an early aftershock? *Journal of Geophysical Research: Solid Earth* **2018**, *123*, 3147–3159.
44. Meng, L.; Ampuero, J.P.; Luo, Y.; Wu, W.; Ni, S. Mitigating artifacts in back-projection source imaging with implications for frequency-dependent properties of the Tohoku-Oki earthquake. *Earth, planets and space* **2012**, *64*, 1101–1109.
45. Bowden, D.C.; Sager, K.; Fichtner, A.; Chmiel, M. Connecting beamforming and kernel-based noise source inversion. *Geophysical Journal International* **2020**, *224*, 1607–1620. <https://doi.org/10.1093/gji/ggaa539>.
46. Guilbert, J.; Vergoz, J.; Schissel  , E.; Roueff, A.; Cansi, Y. Use of hydroacoustic and seismic arrays to observe rupture propagation and source extent of the Mw= 9.0 Sumatra earthquake. *Geophysical research letters* **2005**, *32*.
47. Kennett, B.L.N.; Engdahl, E.R.; Buland, R. Constraints on seismic velocities in the Earth from traveltimes. *Geophysical Journal International* **1995**, *122*, 108–124. <https://doi.org/10.1111/j.1365-246X.1995.tb03540.x>.
48. Delph, J.R.; Abgarmi, B.; Ward, K.M.; Beck, S.L.;   zacar, A.A.; Zandt, G.; Sandvol, E.; T  rkelli, N.; Kalafat, D. The effects of subduction termination on the continental lithosphere: Linking volcanism, deformation, surface uplift, and slab tearing in central Anatolia. *Geosphere* **2017**, *13*, 1788–1805.
49. Ahadov, B.; Jin, S. Present-day kinematics in the Eastern Mediterranean and Caucasus from dense GPS observations. *Physics of the Earth and Planetary Interiors* **2017**, *268*, 54–64.
50. Bartol, J.; Govers, R. A single cause for uplift of the Central and Eastern Anatolian plateau? *Tectonophysics* **2014**, *637*, 116–136.
51. G  vercin, S.E.; Karabulut, H.; Konca, A.  .; DoĒan, U.; Ergintav, S. Active seismotectonics of the East Anatolian fault. *Geophysical Journal International* **2022**, *230*, 50–69.
52. Mahatsente, R.;   nal, G.;   men, I. Lithospheric structure and the isostatic state of Eastern Anatolia: Insight from gravity data modelling. *Lithosphere* **2018**, *10*, 279–290.
53. Schildgen, T.F.; Yildirim, C.; Cosentino, D.; Strecker, M.R. Linking slab break-off, Hellenic trench retreat, and uplift of the Central and Eastern Anatolian plateaus. *Earth-Science Reviews* **2014**, *128*, 147–168.
54. Bayrak, E.; Yilmaz,   .; Softa, M.; T  rker, T.; Bayrak, Y. Earthquake hazard analysis for East Anatolian fault zone, Turkey. *Natural Hazards* **2015**, *76*, 1063–1077.
55. Altunel, E.; Kozacı,   .; Yildirim, C.; Sbeinati, R.M.; Meghraoui, M. Potential domino effect of the 2023 Kahramanmara  earthquake on the centuries-long seismic quiescence of the Dead Sea fault: inferences from the North Anatolian fault. *Scientific Reports* **2024**, *14*, 15440. <https://doi.org/10.1038/s41598-024-65906-4>.
56. Ambraseys, N. *Earthquakes in the Mediterranean and Middle East: a multidisciplinary study of seismicity up to 1900*; Cambridge University Press, 2009.



57. Chen, W.; Rao, G.; Kang, D.; Wan, Z.; Wang, D. Early Report of the Source Characteristics, Ground Motions, and Casualty Estimates of the 2023 Mw 7.8 and 7.5 Turkey Earthquakes. *Journal of Earth Science* **2023**, *34*, 297–303. <https://doi.org/https://doi.org/10.1007/s12583-023-1316-6>.
58. Melgar, D.; Taymaz, T.; Ganas, A.; Crowell, B.W.; Öcalan, T.; Kahraman, M.; Tsironi, V.; Yolsal-Çevikbil, S.; Valkaniotis, S.; Irmak, T.S.; et al. Sub-and super-shear ruptures during the 2023 Mw 7.8 and Mw 7.6 earthquake doublet in SE Türkiye. *Seismica* **2023**, *2*.
59. Melgar, D.; Ganas, A.; Taymaz, T.; Valkaniotis, S.; Crowell, B.W.; Kapetanidis, V.; Tsironi, V.; Yolsal-Çevikbilen, S.; Öcalan, T. Rupture kinematics of 2020 January 24 M w 6.7 Doğanyol-Sivrice, Turkey earthquake on the East Anatolian Fault Zone imaged by space geodesy. *Geophysical Journal International* **2020**, *223*, 862–874.
60. Kusky, T.M.; Bozkurt, E.; Meng, J.; Wang, L. Twin earthquakes devastate southeast Türkiye and Syria: First report from the epicenters. *Journal of Earth Science* **2023**, *34*, 291–296. <https://doi.org/https://doi.org/10.1007/s12583-023-1317-5>.
61. Ishii, M.; Shearer, P.M.; Houston, H.; Vidale, J.E. Teleseismic P wave imaging of the 26 December 2004 Sumatra-Andaman and 28 March 2005 Sumatra earthquake ruptures using the Hi-net array. *Journal of Geophysical Research: Solid Earth* **2007**, *112*.
62. Meng, L.; Inbal, A.; Ampuero, J.P. A window into the complexity of the dynamic rupture of the 2011 Mw 9 Tohoku-Oki earthquake. *Geophysical Research Letters* **2011**, *38*.
63. Bai, K. Dynamic Earthquake Source Modeling and the Study of Slab Effects. PhD thesis, 2019.
64. Wang, D.; Mori, J.; Koketsu, K. Fast rupture propagation for large strike-slip earthquakes. *Earth and Planetary Science Letters* **2016**, *440*, 115–126.
65. Yue, H.; Castellanos, J.C.; Yu, C.; Meng, L.; Zhan, Z. Localized water reverberation phases and its impact on backprojection images. *Geophysical Research Letters* **2017**, *44*, 9573–9580.
66. Huang, B.S.; Chen, J.h.; Liu, Q.; Chen, Y.G.; Xu, X.; Wang, C.Y.; Lee, S.J.; Yao, Z.X. Estimation of rupture processes of the 2008 Wenchuan Earthquake from joint analyses of two regional seismic arrays. *Tectonophysics* **2012**, *578*, 87–97. <https://doi.org/10.1016/j.tecto.2011.12.026>.
67. Sultan, M.; Javed, F.; Mahmood, M.F.; Shah, M.A.; Ahmed, K.A.; Iqbal, T. Imaging of rupture process of 2005 Mw 7.6 Kashmir earthquake using back projection techniques. *Arabian Journal of Geosciences* **2022**, *15*, 871.
68. Kiser, E.; Ishii, M. The 2010 Mw 8.8 Chile earthquake: Triggering on multiple segments and frequency-dependent rupture behavior. *Geophysical Research Letters* **2011**, *38*.
69. Kiser, E.; Ishii, M. The March 11, 2011 Tohoku-oki earthquake and cascading failure of the plate interface. *Geophysical Research Letters* **2012**, *39*.
70. Koper, K.; Hutko, A.; Lay, T. Along-dip variation of teleseismic short-period radiation from the 11 March 2011 Tohoku earthquake (Mw 9.0). *Geophysical research letters* **2011**, *38*.
71. Koper, K.D.; Hutko, A.R.; Lay, T.; Ammon, C.J.; Kanamori, H. Frequency-dependent rupture process of the 2011 M w 9.0 Tohoku Earthquake: Comparison of short-period P wave backprojection images and broadband seismic rupture models. *Earth, planets and space* **2011**, *63*, 599–602.
72. Roten, D.; Miyake, H.; Koketsu, K. A Rayleigh wave back-projection method applied to the 2011 Tohoku earthquake. *Geophysical Research Letters* **2012**, *39*.
73. Wang, D.; Mori, J. Rupture process of the 2011 off the Pacific coast of Tohoku Earthquake (Mw 9.0) as imaged with back-projection of teleseismic P-waves. *Earth, planets and space* **2011**, *63*, 603–607.
74. Wang, D.; Mori, J. Frequency-dependent energy radiation and fault coupling for the 2010 Mw8. 8 Maule, Chile, and 2011 Mw 9. 0 Tohoku, Japan, earthquakes. *Geophysical Research Letters* **2011**, *38*.
75. Yagi, Y.; Nakao, A.; Kasahara, A. Smooth and rapid slip near the Japan Trench during the 2011 Tohoku-oki earthquake revealed by a hybrid back-projection method. *Earth and Planetary Science Letters* **2012**, *355*, 94–101.
76. Yao, H.; Gerstoft, P.; Shearer, P.M.; Mecklenbräuker, C. Compressive sensing of the Tohoku-Oki Mw 9.0 earthquake: Frequency-dependent rupture modes. *Geophysical Research Letters* **2011**, *38*.
77. Meng, L.; Ampuero, J.P.; Sladen, A.; Rendon, H. High-resolution backprojection at regional distance: Application to the Haiti M7. 0 earthquake and comparisons with finite source studies. *Journal of Geophysical Research: Solid Earth* **2012**, *117*.
78. Satriano, C.; Kiraly, E.; Bernard, P.; Vilotte, J.P. The 2012 Mw 8.6 Sumatra earthquake: Evidence of westward sequential seismic ruptures associated to the reactivation of a N-S ocean fabric. *Geophysical Research Letters* **2012**, *39*.
79. Yao, H.; Shearer, P.M.; Gerstoft, P. Subevent location and rupture imaging using iterative backprojection for the 2011 Tohoku M w 9.0 earthquake. *Geophysical Journal International* **2012**, *190*, 1152–1168.

80. Li, B.; Gabriel, A.; Hillers, G. Source Properties of the Induced ML 0.0–1.8 Earthquakes from Local Beamforming and Backprojection in the Helsinki Area, Southern Finland. *Seismological Research Letters* **2024**, *96*, 111–129. <https://doi.org/10.1785/0220240122>.
81. Taylor, G.; Hillers, G.; Vuorinen, T.A.T. Using Array-Derived Rotational Motion to Obtain Local Wave Propagation Properties From Earthquakes Induced by the 2018 Geothermal Stimulation in Finland. *Geophysical Research Letters* **2021**, *48*, e2020GL090403. <https://doi.org/10.1029/2020GL090403>.
82. Gkogkas, K.; Lin, F.; Allam, A.A.; Wang, Y. Shallow Damage Zone Structure of the Wasatch Fault in Salt Lake City from Ambient-Noise Double Beamforming with a Temporary Linear Array. *Seismological Research Letters* **2021**, *92*, 2453–2463. <https://doi.org/10.1785/0220200404>.
83. Gong, J.; McGuire, J.J. Waveform Signatures of Earthquakes Located Close to the Subducted Gorda Plate Interface. *Bulletin of the Seismological Society of America* **2022**, *112*, 2440–2453. <https://doi.org/10.1785/0120210261>.
84. Qin, T.; Lu, L.; Ding, Z.; Feng, X.; Zhang, Y. High-Resolution 3D Shallow S Wave Velocity Structure of Tongzhou, Subcenter of Beijing, Inferred From Multimode Rayleigh Waves by Beamforming Seismic Noise at a Dense Array. *Journal of Geophysical Research: Solid Earth* **2022**, *127*, e2021JB023689. <https://doi.org/10.1029/2021JB023689>.
85. Ammirati, J.B.; Mackaman-Lofland, C.; Zeckra, M.; Gobron, K. Stress transmission along mid-crustal faults highlighted by the 2021 Mw 6.5 San Juan (Argentina) earthquake. *Scientific Reports* **2022**, *12*, 17939.
86. Takano, T.; Poli, P. Coherence-Based Characterization of a Long-Period Monochromatic Seismic Signal. *Geophysical Research Letters* **2025**, *52*, e2024GL113290. <https://doi.org/10.1029/2024GL113290>.
87. Anderson, J.F.; Johnson, J.B.; Mikesell, T.D.; Liberty, L.M. Remotely imaging seismic ground shaking via large-N infrasound beamforming. *Communications Earth & Environment* **2023**, *4*, 399.
88. Blackwell, A.; Craig, T.; Rost, S. Automatic relocation of intermediate-depth earthquakes using adaptive teleseismic arrays. *Geophysical Journal International* **2024**, *239*, 821–840. <https://doi.org/10.1093/gji/ggae289>.
89. Aghaee-Naeini, A.; Fry, B.; Eccles, D. Spatial-Temporal Rupture Characterization of Potential Tsunamigenic Earthquakes Using Beamforming: Faster and More Accurate Tsunami Early Warning; EGU General Assembly 2024, Vienna, Austria, 14–19, 2024.
90. Ammon, C.J.; Ji, C.; Thio, H.K.; Robinson, D.; Ni, S.; Hjorleifsdottir, V.; Kanamori, H.; Lay, T.; Das, S.; Helmberger, D.; et al. Rupture process of the 2004 Sumatra-Andaman earthquake. *science* **2005**, *308*, 1133–1139.
91. Oshima, M.; Takenaka, H.; Matsubara, M. High-Resolution Fault-Rupture Imaging by Combining a Backprojection Method With Binarized MUSIC Spectral Image Calculation. *Journal of Geophysical Research: Solid Earth* **2022**, *127*, e2022JB024003. <https://doi.org/10.1029/2022JB024003>.
92. Zali, Z.; Ohrnberger, M.; Scherbaum, F.; Cotton, F.; Eibl, E.P. Volcanic tremor extraction and earthquake detection using music information retrieval algorithms. *Seismological Research Letters* **2021**, *92*, 3668–3681. <https://doi.org/10.1785/0220210016>.
93. Jian, P.R., Rupture Characteristics of the 2016 Meinong Earthquake Revealed by the Back-Projection and Directivity Analysis of Teleseismic Broadband Waveforms. In *AutoBATS and 3D MUSIC: New Approaches to Imaging Earthquake Rupture Behaviors*; Springer Singapore: Singapore, 2021; pp. 59–72. [https://doi.org/10.1007/978-981-16-5584-5\\_4](https://doi.org/10.1007/978-981-16-5584-5_4).
94. Vera, F.; Tilmann, F.; Saul, J. A Decade of Short-Period Earthquake Rupture Histories From Multi-Array Back-Projection. *Journal of Geophysical Research: Solid Earth* **2024**, *129*, e2023JB027260. <https://doi.org/10.1029/2023JB027260>.
95. Zhang, Y.; Bao, H.; Aoki, Y.; Hashima, A. Integrated seismic source model of the 2021 M 7.1 Fukushima earthquake. *Geophysical Journal International* **2022**, *233*, 93–106. <https://doi.org/10.1093/gji/ggac433>.
96. Bao, H.; Xu, L.; Meng, L.; Ampuero, J.P.; Gao, L.; Zhang, H. Global frequency of oceanic and continental supershear earthquakes. *Nature Geoscience* **2022**, *15*, 942–949.
97. Ni, S.; Kanamori, H.; Helmberger, D. Energy radiation from the Sumatra earthquake. *Nature* **2005**, *434*, 582–582.
98. Stefano, D.; R., C.C.; Chiaraluce, L.; Cocco, M.; Gori, P.D.; Piccinini, D.; Valoroso, L. Fault zone properties affecting the rupture evolution of the 2009 (M 6.1) L'Aquila earthquake (central Italy): Insights from seismic tomography. *Geophysical Research Letters* **2011**, *38*. <https://doi.org/10.1029/2011GL047365>.
99. Chandrakumar, C.; Tan, M.L.; Holden, C.; T., S.M.; Prasanna, R. Performance analysis of P-wave detection algorithms for a community-engaged earthquake early warning system – a case study of the 2022 M5.8 Cook

- Strait earthquake. *New Zealand Journal of Geology and Geophysics* **2025**, *68*, 135–150. <https://doi.org/10.1080/00288306.2023.2284276>.
100. Zhang, D.; Fu, J.; Li, Z.; Wang, L.; Li, J.; Wang, J. A Synchronous Magnitude Estimation with P-Wave Phases' Detection Used in Earthquake Early Warning System. *Sensors* **2022**, *22*. <https://doi.org/10.3390/s22124534>.
  101. Barbot, S.; Luo, H.; Wang, T.; Hamiel, Y.; Piatibratova, O.; Javed, M.T.; Braitenberg, C.; Gurbuz, G. Slip distribution of the February 6, 2023 Mw 7.8 and Mw 7.6, Kahramanmaraş, Turkey earthquake sequence in the East Anatolian fault zone. *Seismica* **2023**, *2*.
  102. Nikolopoulos, D.; Cantzos, D.; Alam, A.; Dimopoulos, S.; Petraki, E. Electromagnetic and Radon Earthquake Precursors. *Geosciences* **2024**, *14*. <https://doi.org/10.3390/geosciences14100271>.
  103. Dunham, E.M.; Archuleta, R.J. Evidence for a supershear transient during the 2002 Denali fault earthquake. *Bulletin of the Seismological Society of America* **2004**, *94*, S256–S268.
  104. Wang, D.; Mori, J. The 2010 Qinghai, China, earthquake: A moderate earthquake with supershear rupture. *Bulletin of the Seismological Society of America* **2012**, *102*, 301–308.
  105. Yue, H.; Lay, T.; Freymueller, J.T.; Ding, K.; Rivera, L.; Ruppert, N.A.; Koper, K.D. Supershear rupture of the 5 January 2013 Craig, Alaska (MW 7.5) earthquake. *Journal of Geophysical Research: Solid Earth* **2013**, *118*, 5903–5919.
  106. Zhan, Z.; Helmberger, D.V.; Kanamori, H.; Shearer, P.M. Supershear rupture in a Mw 6.7 aftershock of the 2013 Sea of Okhotsk earthquake. *Science* **2014**, *345*, 204–207.
  107. Xia, K.; Rosakis, A.J.; Kanamori, H.; Rice, J.R. Laboratory earthquakes along inhomogeneous faults: Directionality and supershear. *Science* **2005**, *308*, 681–684.
  108. Zhang, H. *Imaging the Rupture Processes of Earthquakes Using the Relative Back-Projection Method: Theory and Applications*; Springer, 2017.

**Disclaimer/Publisher's Note:** The statements, opinions and data contained in all publications are solely those of the individual author(s) and contributor(s) and not of MDPI and/or the editor(s). MDPI and/or the editor(s) disclaim responsibility for any injury to people or property resulting from any ideas, methods, instructions or products referred to in the content.